buildings

Article

Cyclic Behavior of Slab–Wall Connections with Concrete-Filled Steel Tubes Embedded in Wall Piers

Kai-Min Chen [1], Fan Wang [2,3,*], Xiao-Dan Fang [3], Hua-Ming Zeng [1] and Xie-Sheng Li [1]

1 School of Civil Engineering & Transportation, South China University of Technology, Guangzhou 510461, China; 202021009312@scut.edu.cn (K.-M.C.); zenghm@gddholdings.com (H.-M.Z.); 201721007860@scut.edu.cn (X.-S.L.)
2 State Key Laboratory of Subtropical Building Science, South China University of Technology, Guangzhou 501641, China
3 Architectural Design & Research Institute of SCUT Co., Ltd., South China University of Technology, Guangzhou 501641, China; f5101@126.com
* Correspondence: wangfan@scut.edu.cn; Tel.: +86-137-1033-8386

Abstract: Concrete-filled steel tubes (CFSTs) embedded in structural walls can improve the lateral-force resistance of slab–wall structures, but also impede the passage and anchorage of steel bars in slabs around the tubes. Therefore, the objective of this research is to propose the design of anchorage detailing to solve this problem, and analyze the bearing capacity and seismic performance of the joint using this design. Two types of no-through-tube anchorage detailing were put forward for steel bars in slabs that intersect with CFST-strengthened structural walls: (1) an anchoring ring (AR) detailing; (2) a direct anchoring (DA) detailing. Four slab–wall concrete specimens using these two detailing types were tested cyclically. It was found that the connection specimens with the AR detailing had better ductility and energy dissipation capacity compared to those with the DA detailing. Nevertheless, the connection specimens with the DA detailing had more direct force-transferring capacities, meaning that they were better at transferring the force received by the slabs to the shear walls. Overall, both types of detailing can be adopted in practice to significantly improve the seismic performance of slab–wall connections, and the choice of which to use would depend on the specific requirements of a project.

Keywords: CFST shear wall–slab joints; cyclic loading; failure mechanism; seismic capacity

check for updates

Citation: Chen, K.-M.; Wang, F.; Fang, X.-D.; Zeng, H.-M.; Li, X.-S. Cyclic Behavior of Slab–Wall Connections with Concrete-Filled Steel Tubes Embedded in Wall Piers. *Buildings* **2023**, *13*, 1453. https://doi.org/10.3390/buildings13061453

Academic Editor: André Furtado

Received: 1 May 2023
Revised: 14 May 2023
Accepted: 20 May 2023
Published: 2 June 2023

Copyright: © 2023 by the authors. Licensee MDPI, Basel, Switzerland. This article is an open access article distributed under the terms and conditions of the Creative Commons Attribution (CC BY) license (https://creativecommons.org/licenses/by/4.0/).

1. Introduction

By eliminating beams and columns, the use of a slab–wall system in structural engineering has gained traction due to the benefits of increased unobstructed room height and improved construction efficiency. However, the absence of those elements results in shear walls bearing both vertical and horizontal loads, leading possibly to a significant reduction in the seismic performance of the system. In particular, experiments [1–3] have identified that the slab–wall joints in the system are the weakest link. Various solutions have been proposed to enhance the system or shear walls alone. Among them, adding concrete-filled steel tubes (CFSTs) in shear wall piers has emerged as an effective means.

Qian [4] proposed a shear wall with CFSTs embedded at the wall boundary, which was found to offer excellent energy dissipation capacity. Fang's group has studied the effects of various loading conditions on shear walls embedded with CFSTs, including axial compression, axial compression plus bending actions, cyclic loads, shearing, and combined tension-shearing [5–9]. The results show that in CFST-strengthened shear walls, the steel tubes provide a confinement effect that significantly improves the strength of the shear walls. Furthermore, the embedded CFSTs can delay local failures of the wall by increasing its vertical load-bearing capacity, thus creating a shear wall with higher rigidity and good ductility. Ji and his collaborators [10] developed a numerical-simulation model of high-strength CFST-strengthened shear walls to examine their behavior when subjected to high axial force and lateral cyclic loading. The results indicate that the walls' flexural strength increases with the increasing ratio of the cross-sectional area of embedded tubes. Notably, the type of embedded tubes, whether empty or concrete-filled, did not affect the walls' strength. Wu [11] proposed a precast composite shear wall with steel tubes embedded at the wall boundary, and found this new kind of component can be applied in a precast building to improve its structural performance. Similarly, Zhou et al. [12] designed a precast concrete-encased CFST composite wall with twin steel-tube connections, and their work resulted in several calculation methods for evaluating the shear strength of the wall. Zhao et al. [13] had been studied on a shaking table testing of a 1/8-scale five-story slab–wall structure equipped with CFSTs in walls. Findings indicated that the application of CFSTs was instrumental in resisting the simulated earthquake loads acting upon it, hence the global response limits required by codes of practice were met. Nevertheless, the junctions between the shear walls and floor slabs were found to be the weakest links in the whole system. Consequently, it suggested designers should use proper detailing in those regions to prevent local distress.

These studies indicate that incorporating CFSTs into slab–wall structures has the potential to enhance their seismic performance. However, because the double-layer bidirectional steel bars in the slab are difficult to pass through the steel tubes equidistantly arranged in the shear wall, the steel bars are bent or directly penetrate by drilling holes to make them pass through the steel tubes in the relevant research. Such a method will affect the material properties of steel bars and steel tube at the joint, making it unable to fully play its role.

It can be seen that the use of CFST in a slab–wall system has been limited due to the complexity of the slab-to-shear wall piers connections and the blank of design of anchorage detailing. In addition, there is still a lack of information on CFST connections embedded in wall piers under cyclic loading. Therefore, developing a practical connection to overcome these challenges is crucial.

To address these issues, the purpose of the study is to design no-through-tube anchorage detailing for steel bars in slabs that intersect with CFST-strengthened structural walls, and investigate the influence of using this different anchoring detailing in slab–wall joints on strength, ductility, stiffness, and energy dissipation. A higher grade of concrete is used inside the steel tube than the slab to prevent it from failing prematurely due to hooping effect.

It is believed that the outcomes of this work will contribute to the understanding of the overall seismic performance of the slab–wall systems concerned, and, ultimately, promote the application of the highly ductile wall components embedded with CFSTs in the future work.

2. Experimental Program

2.1. Specimen Design

A 3D view of this structure is displayed in Figure 1. The prototype structure has five stories with a total height of 30 m, 6 m high for each story. Figure 2 shows the plan layout of a typical floor of the prototype structure adopted in the joint design and test in this paper. All of the floor slabs are of the same thickness, 150 mm, and have the role of coupling all the wall piers with specially-shaped cross sections ('L' or 'T').

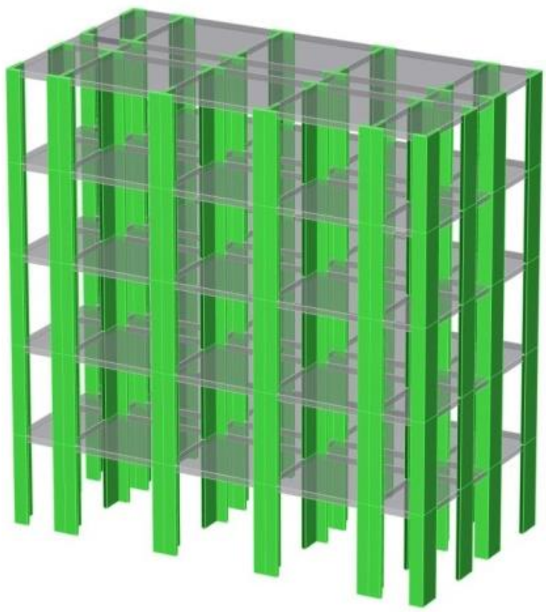

Figure 1. 3D rendering of the prototype structure.

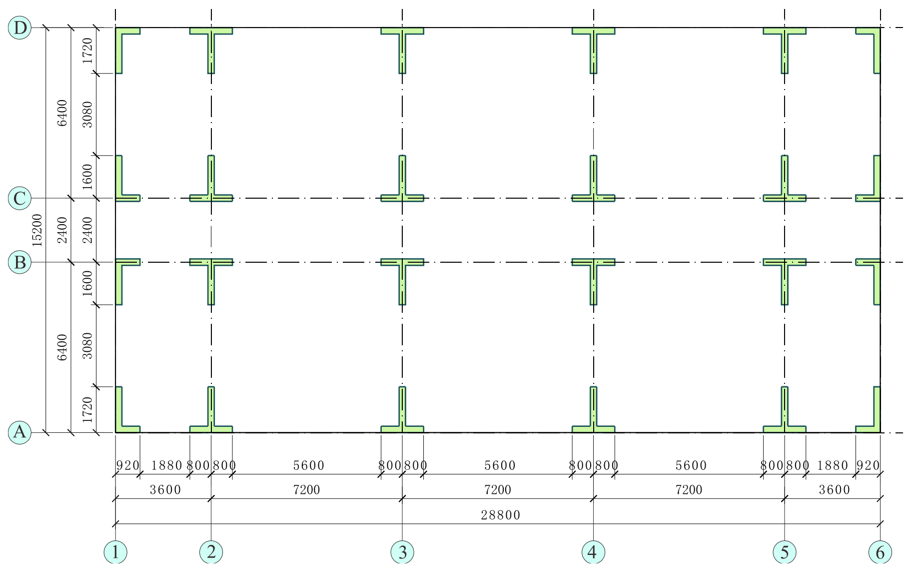

Figure 2. Plan layout of the prototype structure (unit: mm).

Two types of no-through-tube anchorage detailing are purposed in this paper. The first method is the anchoring ring (AR) detailing, shown in Figure 3a,b, which involves placing two layers of steel anchoring rings around a steel tube embedded in the shear wall. The steel bars in the floor slab that are obstructed by the tube are bent into a U-shape, interlocking with the rings to transfer the force between the slab and the tube. The second method is the direct anchoring (DA) detailing, as shown in Figure 3c,d, which removes the floor slab's steel bars that are blocked by the tube, allowing the remaining bars to bypass the tube. These orthogonal direct anchoring bars are placed to surround the steel tube.

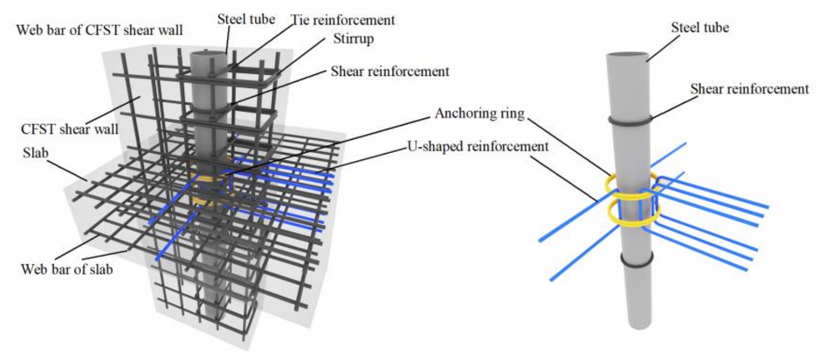

(**a**) 3D diagram of anchoring rings (AR) detailing.

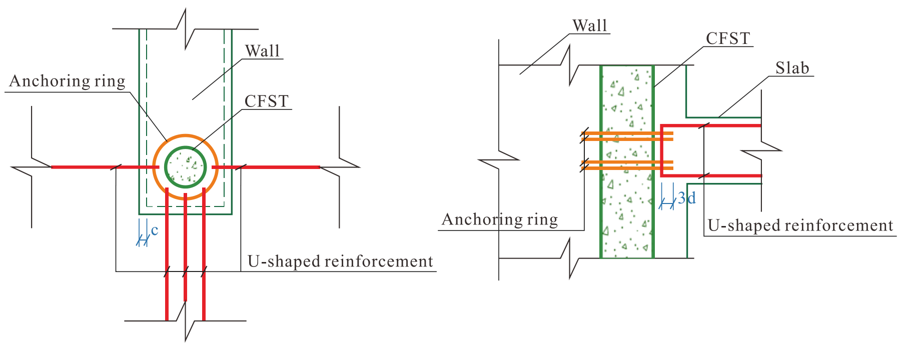

(**b**) anchoring rings (AR) detailing.

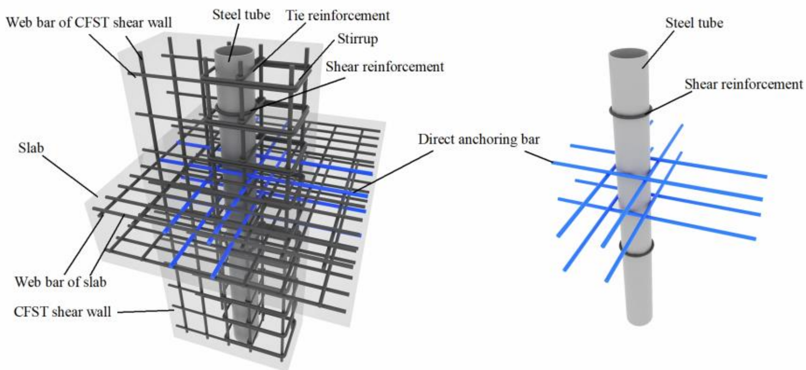

(**c**) 3D diagram of direct anchoring (DA) structure.

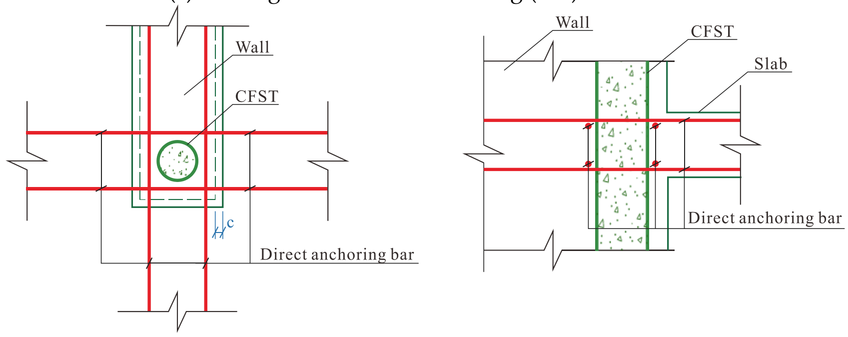

(**d**) direct anchoring (DA) structure.

Figure 3. Geometry of the anchorage method in CFST wall—slab joints.

In order to investigate the seismic performance of the AR and DA anchorage detailing methods, cyclic-loading experiments were carried out on four subassemblies of I- and T-shaped slab–walls reinforced with CFSTs. The findings showed that the incorporation of these anchorage methods allowed for effective transmission of bending moments in the floor slab of the CFST-strengthened structure, resulting in the formation of plastic hinges under cyclic loading. This research is anticipated to aid in the adoption of CFST-strengthened slab-wall structures and contribute to the creation of a highly ductile structural system.

The prototype structure had 2 specially-shaped cross sections ('L' or 'T'), adopting the thickness of 200 mm. Therefore, based on this modeling, the shear wall of each specimen had an "I-shaped" or "T-shaped" configuration. The specimens were named SW1, SW2, TW1, and TW2. The slab–wall joints of the structure were truncated at the reverse bending point and taken out as a specimen for cyclic test. The transverse span of the slab was appropriately increased for better simulation [14], so the length of slabs was 1800 mm and the effective width was 1500 mm.

Figure 4 displays the specimens' shape and size. The tests applied a cyclic push–pull force to the slab, and an axial load to the shear wall. The wall thickness was consistently 200 mm. The floor slab was constructed with C30 concrete, while C60 concrete was utilized for the shear wall. HRB400 steel bars (hot-rolled ribbed bars, C) [15] were used for reinforcement.

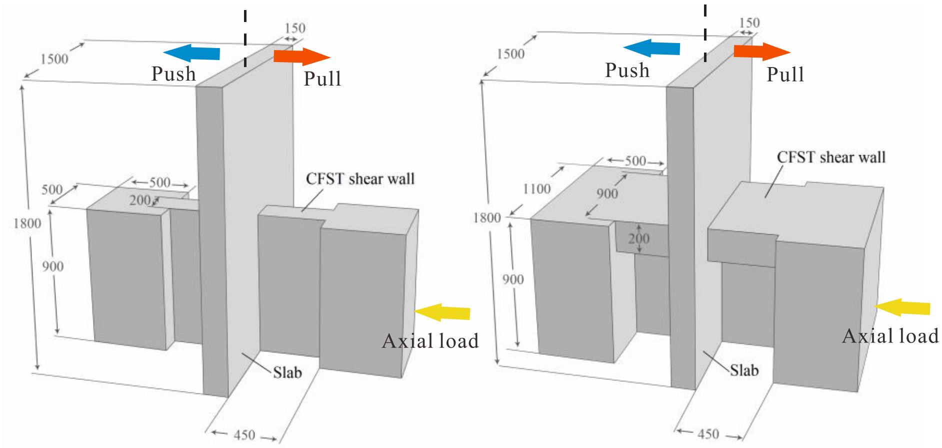

(**a**) SW1 and SW2. (**b**) TW1 and TW2.

Figure 4. Dimensions details of the specimens (unit: mm).

The experimental research parameters applied to the CFST shear wall were given in Table 1.

Table 1. Experimental research parameters.

Specimen Label	Structural Form	The Section of CFST Shear Wall	AR Detailing			DA Detailing		Axial Load N_t (*kN*)
			Group Number	Diameter of Rings (mm)	Diameter of U-Shaped Bars (mm)	Group Number	Diameter of Additional Orthogonal Bars (mm)	
SW1	AR	I-shaped	2	140	8	-	-	1253
SW2	DA	I-shaped	-	-	-	1	10	1253
TW1	AR	T-shaped	6	140	8	-	-	2276
TW2	DA	T-shaped	-	-	-	3	10	2276

The specific configurations of the specimens are shown in Figure 5. The steel tube of the CFSTs embedded in the walls was A 89/81 (the outermost diameter was 89 mm, and the thickness was 8 mm). Shear reinforcement C6@300 was welded on the tube to enhance the composite action between the tube and concrete.

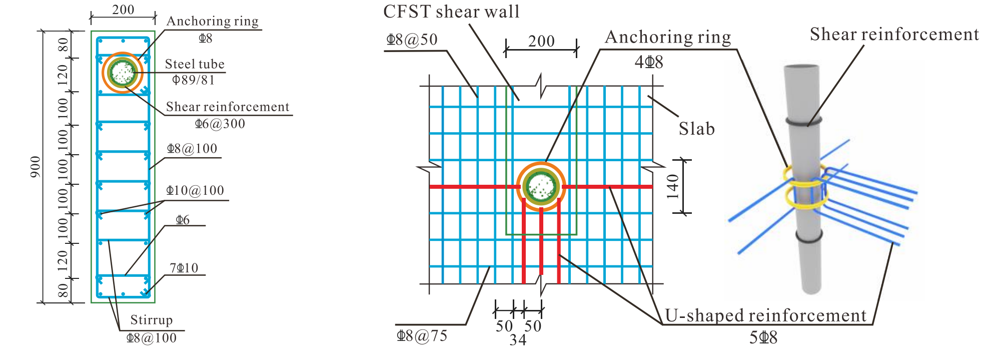

(**a**) Reinforcement details of SW1

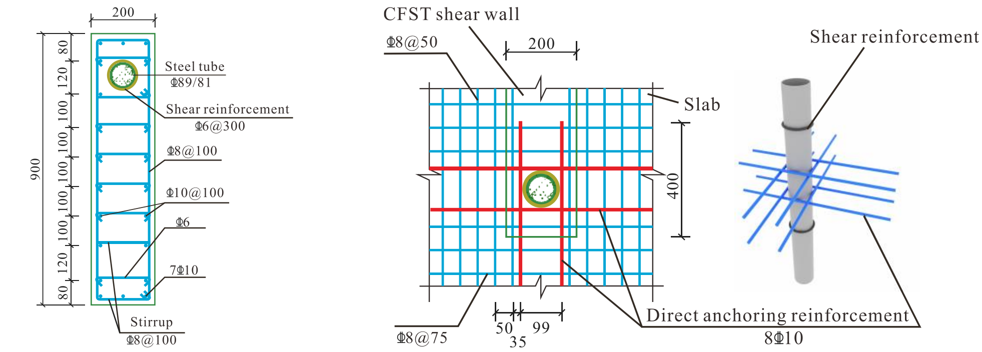

(**b**) Reinforcement details of SW2

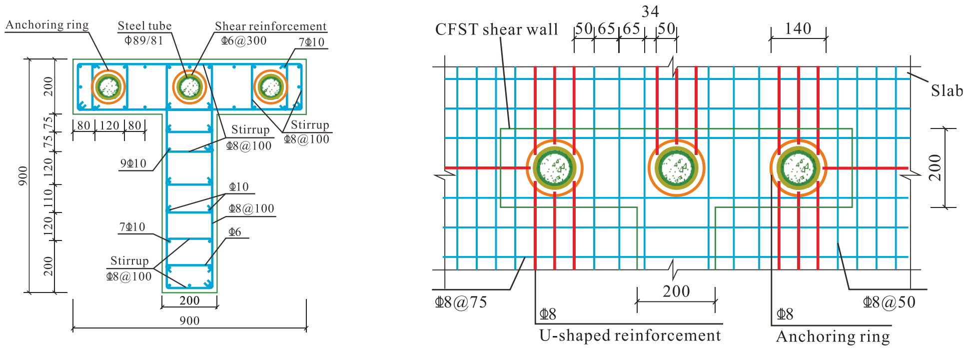

(**c**) Reinforcement details of TW1

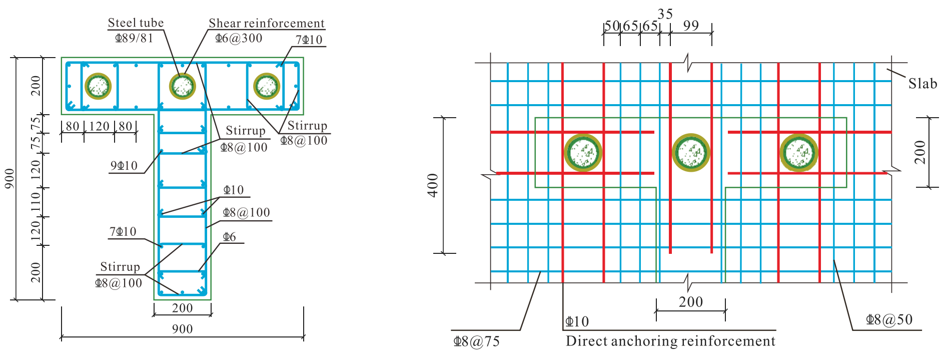

(**d**) Reinforcement details of TW2

Figure 5. Reinforcement details of the specimens (unit: mm).

The SW1 and TW1 specimens used the AR detailing, consisting of two groups of anchoring rings. Each group of the AR reinforcement used 2C8 steel bars to form a double-layer ring with a 140-mm outer diameter. The slab's U-shaped reinforcement was 3C8, connecting to the ARs.

The SW2 and TW2 specimens used the DA detailing, with a steel bar diameter of 10mm. To ensure that the steel reinforcement rate remained unchanged, the steel bars in the slab near the joint region were changed from 3C8 used for the AR detailing to 2C10 in the current case.

2.2. Material Test

Complying with GB50010 [15], 3 standard cubic concrete blocks with side lengths of 150 mm were prepared for compressive strength tests. The results are shown in Table 2.

Table 2. Measured mechanical properties of concrete.

Concrete Type	Location	Cube Compressive Strength (MPa)	Nominal Compressive Strength (MPa)	E_c (GPa)
C30	Floor slab	44.6	27.3	32.8
C60	CFST shear wall	63.8	37.7	36.0

The measured mechanical properties of the steel bars are listed in Table 3, complying with the test standard GB/T 228.1-2010 [16].

Table 3. Measured strength of steel materials.

Steel Type	Yield Strength (MPa)	Ultimate Strength (MPa)
C 8 steel bar	443	637
C 10 steel bar	528	631
C 22 steel bar	457	602
Steel tube	378	534

2.3. Experimental Setup

The test setup and instrumentation are shown in Figure 6. The ends of the shear wall were fixed, while a cyclic load was applied to the slab. Before the test, an axial load was applied by an actuator, remaining constant during the whole experiment.

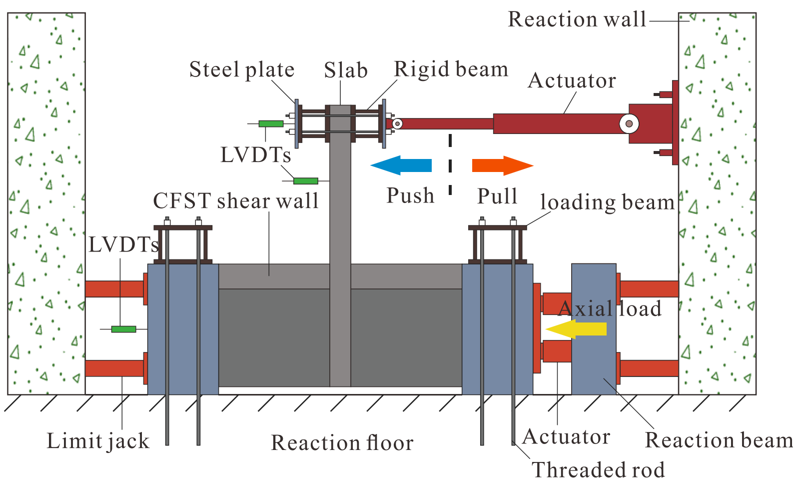

(**a**) Schematic diagram

Figure 6. *Cont.*

(**b**) Photograph.

Figure 6. Test setup for CFST-enhanced slab–wall connections.

Referring to JGJ 101-1996 [17], the loading procedure involved two stages, which are presented in Figure 7. Prior to yielding, the load was incrementally increased by 10 kN. Following yielding, the specimens were subjected to displacement reversals. The loading was stopped either when the specimen suffered severe damage or when its load-bearing capacity fell to approximately 85% of the peak load.

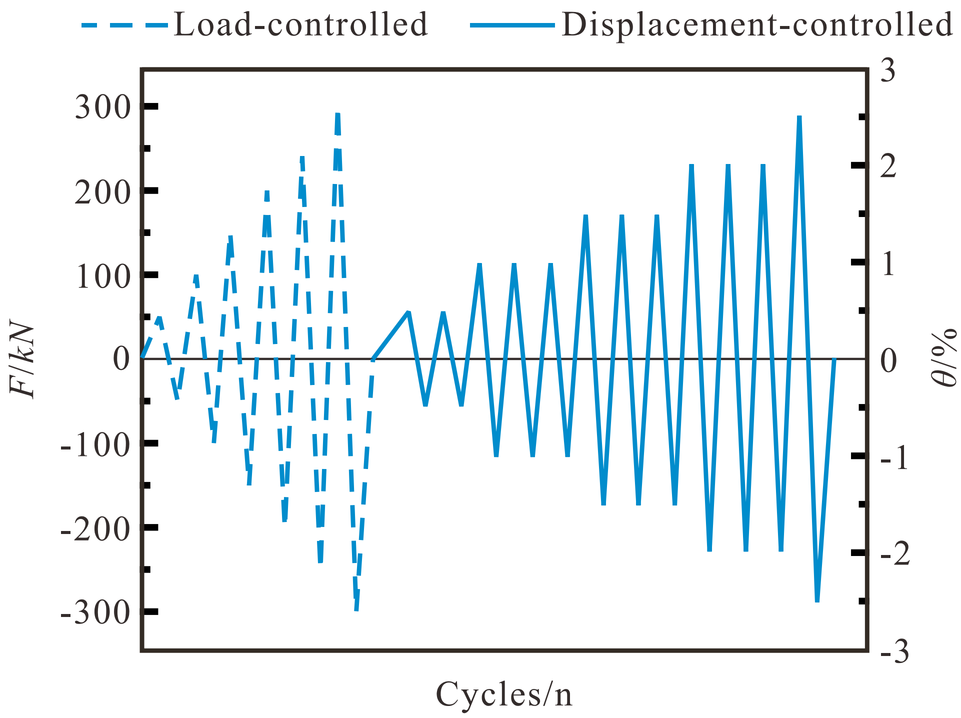

Figure 7. Loading program.

3. Test result and Analysis

3.1. Experimental Observation

The failure processes of the specimens are shown in Figure 8a–d. In these drawings, the cracks are represented in red. The final failure modes of the east and west surfaces of the specimens are shown in Figure 9.

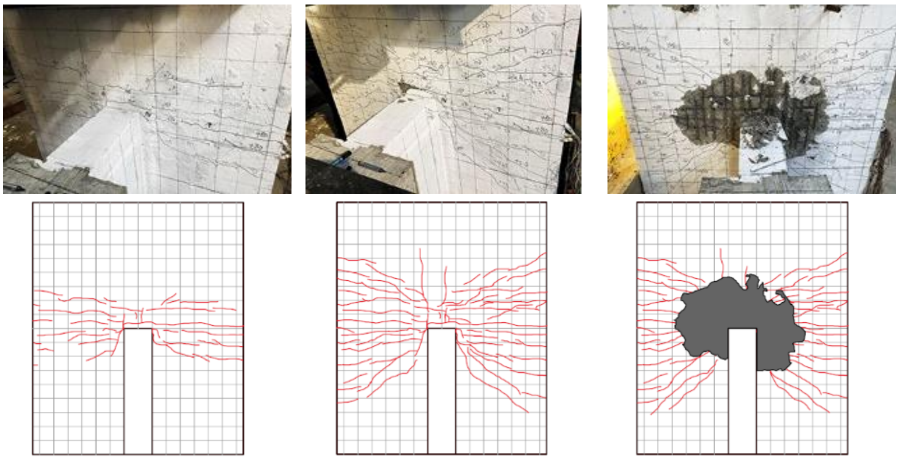

θ = 0.52% θ = 2.08% θ = 5.76%

(**a**) SW1

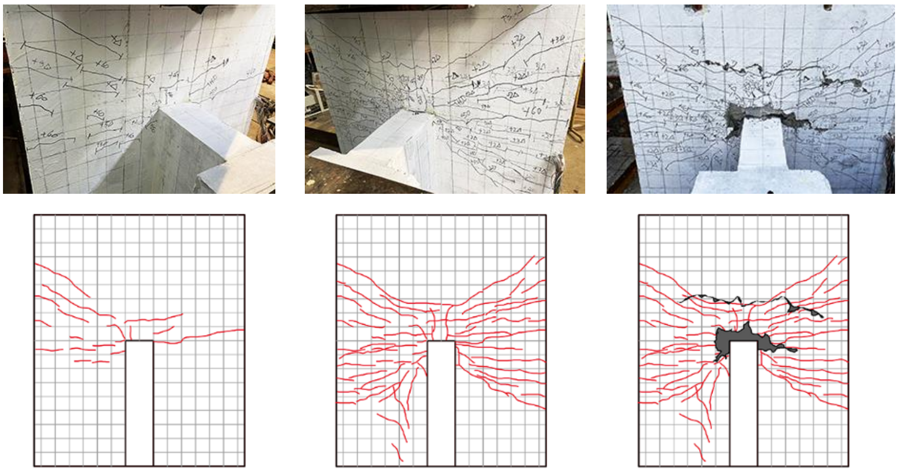

θ = 0.45% θ = 1.81% θ = 4.58%

(**b**) SW2

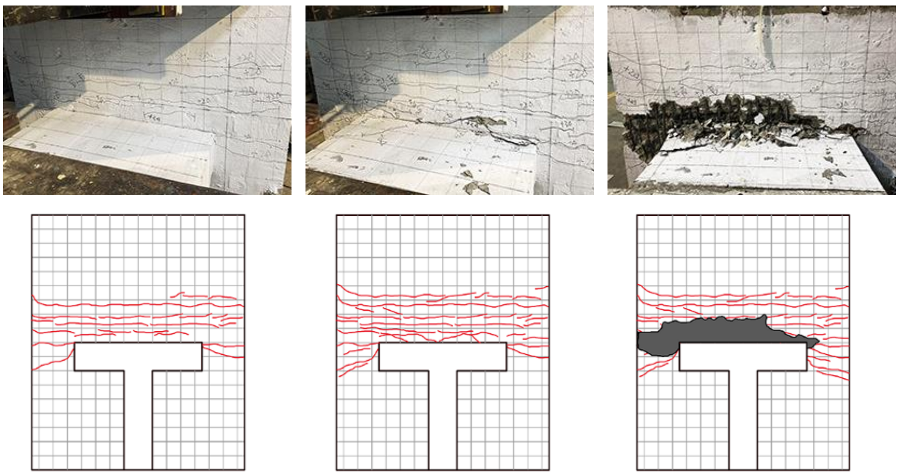

θ = 0.78% θ = 2.34% θ = 5.44%

(**c**) TW1

Figure 8. *Cont.*

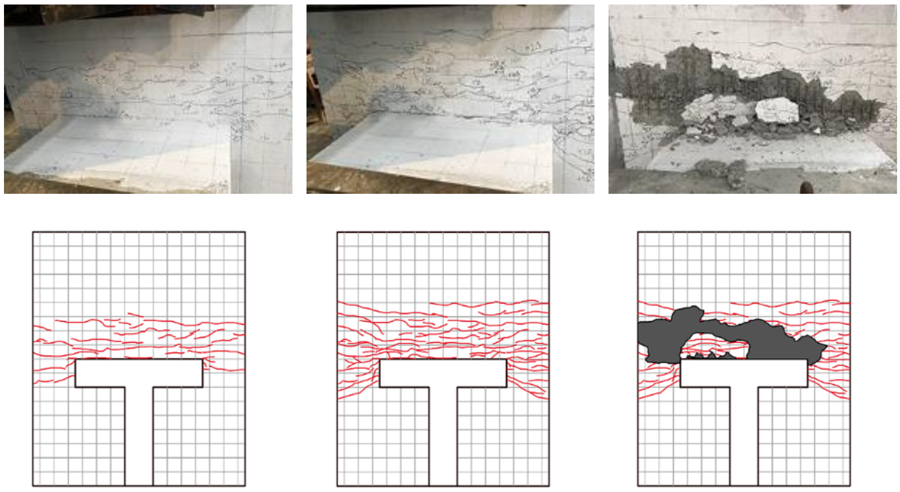

θ = 0.51% θ = 2.60% θ = 4.15%

(**d**) TW2

Figure 8. Failure process of specimens during the testing.

SW1 SW2 TW1 TW2

(**a**) Front view

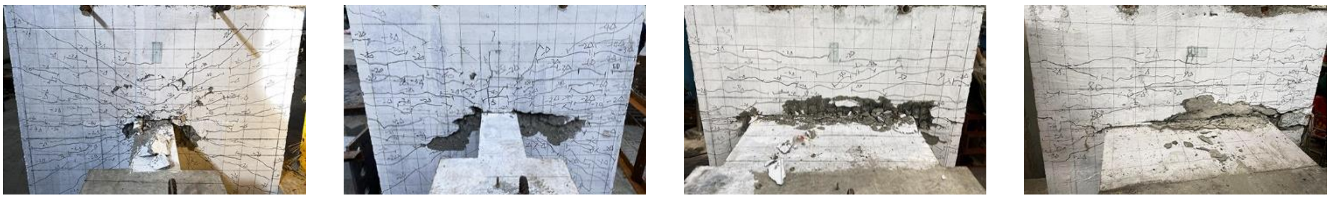

SW1 SW2 TW1 TW2

(**b**) Back view

Figure 9. Failure model of specimens.

After analyzing the failure process and modes of all specimens (as shown in Figures 8 and 9), it can be concluded that the onset of floor slab cracking in the specimens with the AR detailing, namely SW1 and TW1, was delayed compared to those with the DA detailing, namely SW2 and TW2. Notably, the onset of slab cracking in TW1 lagged significantly behind that of TW2, demonstrating that the implementation of the AR detailing in the T-shaped shear wall joint postponed the concrete cracking of the slab. The Ars were situated on the force-transmission path, allowing for the efficient transfer of the tensile force of the slab's steel reinforcing bar to the AR bars, which then conveyed the force to the confined concrete area of the steel tubes. The confined core had substantial rigidity, tensile strength, and pull-out resistance, which the anchoring form of the U-shaped steel bar for the AR detailing could exploit effectively, making the anchoring strength of the AR detailing stronger than that of the DA detailing. Under the influence of the anchoring ring, the joint's failure area expanded, deepening the failure level of SW1 and TW1 specimens compared to the DA detailing.

Due to the support of the rectangular shear-wall boundary with the floor slab, the stress flowing between the rigid beam and the junction became "O"-shaped. The cracks on the floor surface eventually form a radial distribution starting from the edge of the shear wall, because the direction of the cracks in the concrete was perpendicular to the direction of the stress flow.

Since the slab reinforcement ratio of the specimens was consistent, the change of steel anchorage detailing did not significantly affect the peak load of the four specimens. The cracks in all other areas, except the supporting end of the shear wall, were horizontal, exhibiting an evident bending failure mode.

3.2. Load-Displacement Curves

Figure 10 shows the load–drift hysteresis curve of each specimen. It can be observed that all the specimen curves had a gentle falling section after reaching their peak values. In the later stages of loading, all four specimens exhibited a slight degree of pinching due to significant concrete cracking. However, compared to the specimens with the DA detailing (SW2 and TW2), the specimens with the AR detailing (SW1 and TW1) showed a relatively smaller pinching effect and a more complete hysteretic curve.

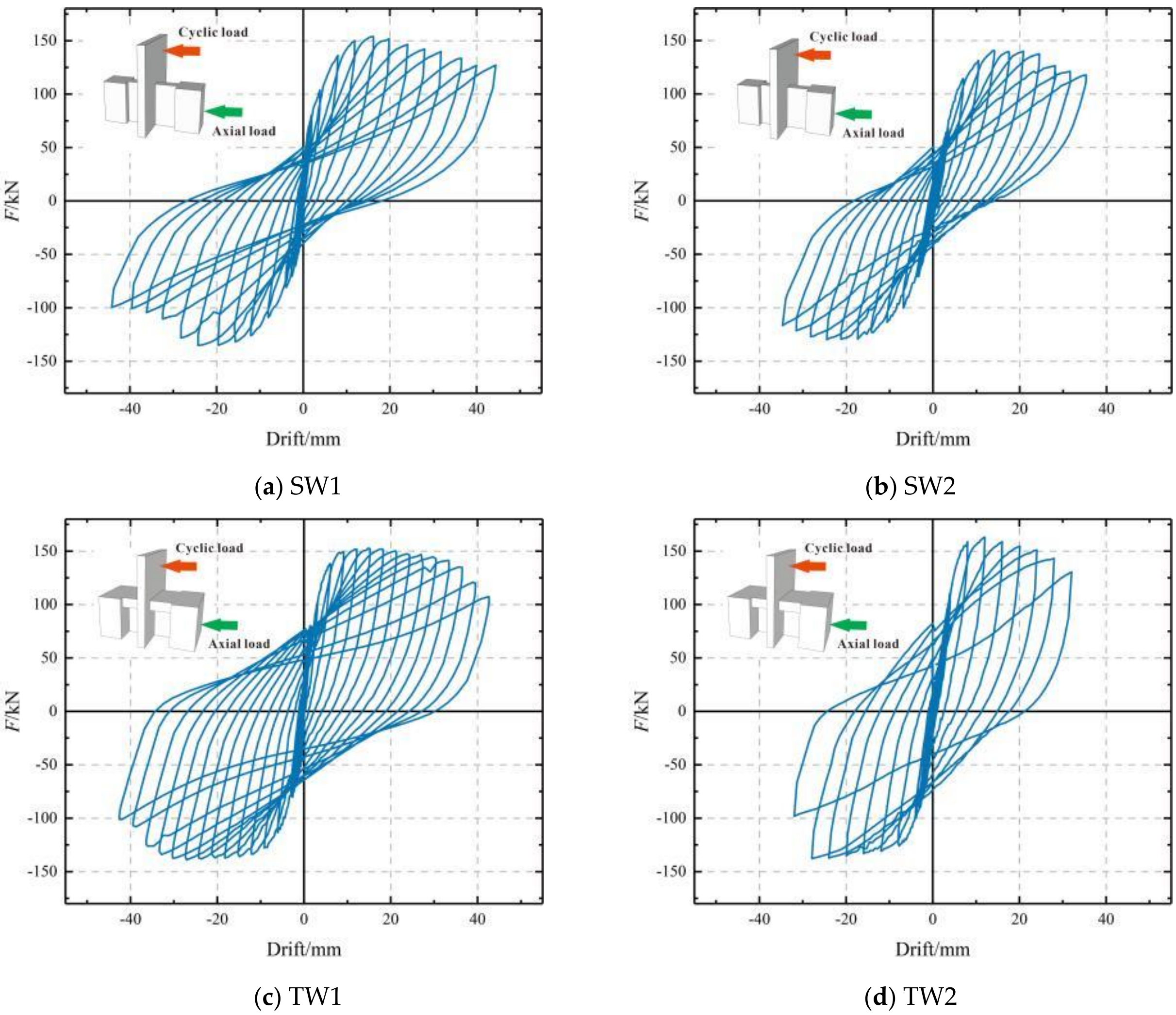

Figure 10. Hysteretic curves of all specimens.

After yielding, the hysteresis curves of the I-shaped section specimens SW1 and SW2 became narrower, while the curves of the T-shaped section specimens TW1 and TW2 were fuller. This suggests that the energy consumption capacity of the T-shaped sectional shear wall specimens is stronger than that of the I-shaped shear wall specimens.

Figure 11 illustrates the skeleton curve of all specimens. As the reinforcement ratio of the specimen floor was the same, the peak load of the four specimens did not show significant changes due to differences in joint structure and supporting conditions of the floor root. When comparing the descending section of the skeleton curve, it was found that although specimens SW1 and TW1 had a gentler decline compared to specimens SW2 and TW2, the bearing capacity and stiffness of all the specimens did not degrade rapidly. During the entire loading process, the AR bars of test pieces SW1 and TW1 remained inside the concrete, while the DA bars of test pieces SW2 and TW2 did not get pulled out.

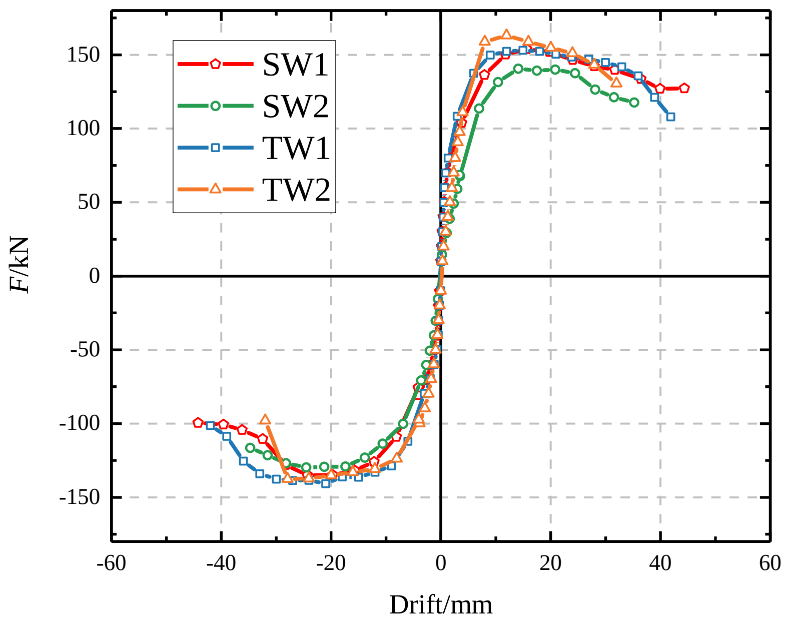

Figure 11. Skeleton curves of specimens.

3.3. Bearing Capacity and Deformation Capacity

Ductility refers to the ability of a structure or component to maintain sufficient bearing capacity after yielding and possess ample plastic deformation capacity before reaching its ultimate bearing capacity. This is an important parameter for evaluating the deformation capacity and seismic performance of the structure or component. In this study, the ductility coefficient (μ) is utilized to quantitatively measure the ductility of the joint specimen. A higher value of the ductility coefficient indicates a greater deformation and energy dissipation capacity of the structure or specimen. The ductility coefficient is calculated using the formula provided in references [18,19], and is averaged between the forward and backward directions.

$$\mu = \frac{\Delta_u}{\Delta_y} \tag{1}$$

where Δ_u is the displacement of the ultimate point corresponding to the load-bearing capacity of the specimen when it falls to 85% of the peak bearing capacity, and Δ_y is the displacement of the yield point, which is calculated by adopting the Park method [20]. The selection of each feature point is shown in Figure 12.

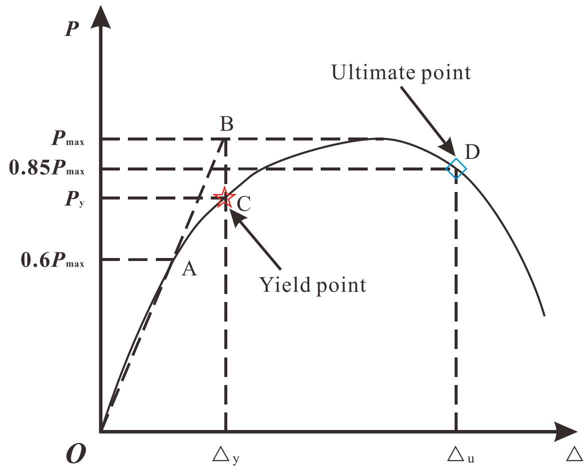

Figure 12. Schematic diagram of yielding point and ultimate point.

Table 4 lists the test results of each characteristic point of the specimen. Among them, V represents the load of the loading point; Δ represents the displacement of the loading point; θ represents the drift of the loading point, $\theta = \Delta/H$; the subscripts cr, y, m, u respectively represent the characteristic points: cracking, yielding, peak, ultimate.

Table 4. Test results of specimens at main stages.

Name	Direction	Crack Point		Yield Point			Peak Point			Ultimate Point			Ductility Factor	
		V_{cr} (kN)	Δ_{cr} (mm)	V_y (kN)	Δ_y (mm)	θ_y	V_m (kN)	Δ_m (mm)	θ_m	V_u (kN)	Δ_u (mm)	θ_u	μ	Mean
SW1	+	50.21	0.67	115.0	5.25	1/147	153.9	15.64	1/49	130.8	37.92	1/20	7.2	5.41
	–	50.53	1.28	111.7	8.72	1/88	135.1	24.30	1/32	114.8	31.42	1/25	3.6	
SW2	+	38.80	1.62	124.7	9.01	1/85	140.5	14.13	1/54	119.5	33.40	1/23	3.7	4.01 *
	–	40.26	1.25	104.5	8.05	1/96	129.8	24.52	1/31	116.5	34.71 *	1/22	4.3	
TW1	+	59.86	0.68	115.6	3.74	1/206	153.1	14.97	1/51	130.1	37.09	1/21	9.9	7.87
	–	59.94	1.19	114.2	6.36	1/121	140.8	20.97	1/37	119.7	36.99	1/21	5.8	
TW2	+	19.94	0.53	133.2	5.85	1/132	163.1	11.98	1/64	138.6	29.42	1/26	5.0	5.84
	–	19.92	0.19	100.8	4.52	1/170	137.6	27.91	1/28	117.0	30.03	1/26	6.6	

*: At the last displacement loading, the negative bearing capacity only decreased to 89.8% of the peak value, which meant the actual deformation capacity of the specimen exceeded this value.

As can be seen from this table, the drifts at the ultimate points g are from 1/26~1/20. Moreover, the ductility coefficients are from 4.01~7.87, all of which meets the requirement that the ductility coefficient should not be less than 3.0 in the seismic design [21]. It proves that the two detailing measures proposed in this study have good seismic performance and deformability.

When comparing specimens with different structural details, it is observed that the ductility coefficients of specimens SW1 and TW1 with the AR detailing are higher than those of specimens SW2 and TW2 with the DA detailing. Furthermore, it can be inferred that specimens TW1 and TW2 with a T-shaped shear wall have higher ductility coefficients than those with an I-shaped cross-section.

3.4. Stiffness Degradation

The reduction in stiffness in a structure or element as the number of low cyclic loads increases is referred to as stiffness degradation. In this study, the secant stiffness, K [22] is employed to assess the stiffness degradation of the specimen during the experiment. The secant stiffness is calculated by dividing the average value of the forward and reverse loads by the average value of the corresponding forward and reverse displacements.

$$K_\mathrm{i} = \frac{(|F_\mathrm{i}^+| + |F_\mathrm{i}^-|)}{(|\Delta_\mathrm{i}^+| + |\Delta_\mathrm{i}^-|)} \tag{2}$$

where F_i^+ and F_i^- are the positive peak load and negative peak load of the *i*th loading cycle, Δ_i^+ and Δ_i^- are the positive peak displacement and negative peak displacement of the ith loading cycle.

Figure 13 presents the test results, showing that the stiffness degradation trends of all four specimens were similar. This implies that the stiffness degradation trend is not significantly influenced by the form of the shear wall or the structural configuration of the joint. Among the specimens, SW2 had the lowest stiffness, while TW2 had the highest stiffness, indicating that the specimen with the AR detailing and the T-shaped shear wall at the bottom plate had a greater stiffness.

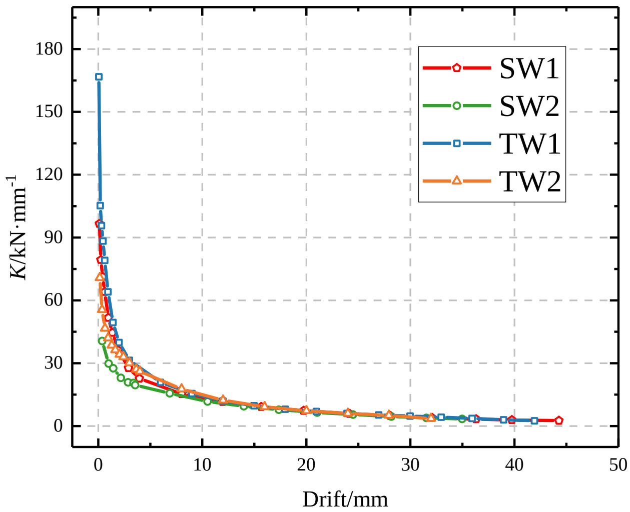

Figure 13. Stiffness degradation curves of all specimens.

Moreover, the stiffness degradation rate of the specimens was positively correlated with the development trend of cracks. As cracks developed faster, the stiffness degradation rate also increased. Numerous cracks appeared and developed rapidly before the specimens yielded, and, during this process, the stiffness of the specimens deteriorated rapidly. However, after the specimens yielded, fewer new cracks appeared, and the stiffness degradation slowed down.

3.5. Cumulative Dissipated Energy

To analyze the energy dissipation performance of the shear-wall specimen, the energy dissipation coefficient, E, is employed. A larger value of E indicates a better energy-dissipation capability of the specimen. As shown in Figure 14a, the following formula is used to calculate the energy dissipation coefficient [21,22]:

$$E = \frac{S_\mathrm{ABC} + S_\mathrm{ACD}}{(S_\mathrm{OBE} + S_\mathrm{ODF})} \tag{3}$$

where S_ABC + S_ACD was the energy absorbed by the component during this cycle of cyclic loading. S_OBE + S_ODF: the total deformation energy of the component during this cycle of cyclic loading.

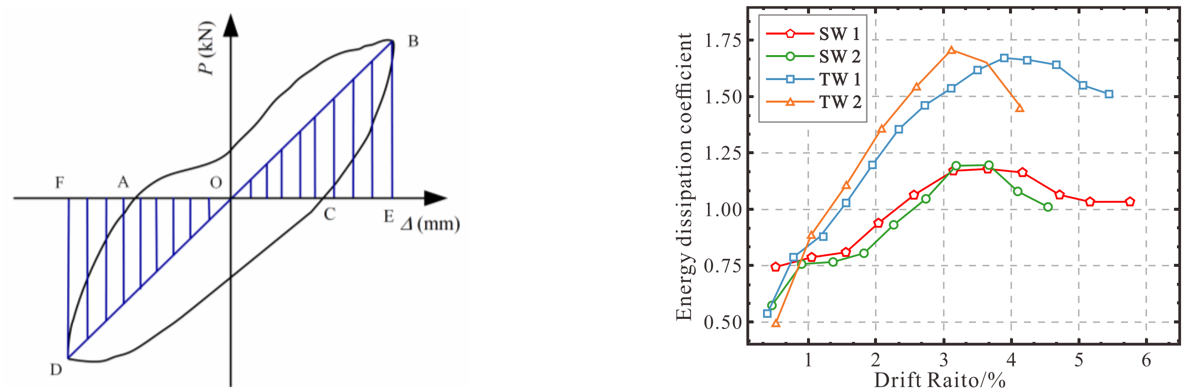

(**a**) Schematic diagram of the calculation of equivalent viscous damping ratio.

(**b**) The relationship between the equivalent viscous damping ratio and displacement of all specimens.

Figure 14. Cumulative dissipated energy.

Figure 14b displays the test results, indicating that the specimens with the AR detailing (SW1 and TW1) had better energy dissipation performance before and after yielding compared to those with the DA detailing (SW2 and TW2) for the same shear wall form. The AR detailing ensured a slow decline in energy consumption capacity after reaching the peak, demonstrating stable energy dissipation performance, while the DA detailing had a weaker ability to delay the decline. In addition, the energy dissipation capacity of specimens TW1 and TW2 was better than that of specimens SW1 and SW2, highlighting that T-shaped shear walls with a larger supporting range exhibit stronger energy dissipation capabilities.

3.6. Strain of the Reinforcements

Figure 15 displays the strain measuring points' arrangement for the 4 specimens. As specimens TW1 and TW2 were symmetric, strain gauges were only placed on the structural area's middle part and one of the ends of the shear wall (Figure 15a,b). In each group of the AR detailing, there were 5 measuring points on the anchor ring and 1 measuring point on the U-shaped reinforcement of specimens SW1 and TW1 (Figure 15c). For the DA detailing, strain gauges were positioned 150 mm and 250 mm away from the shear wall's outer layer to assess the reliability of the DA steel bar's force transmission in the concrete of the shear wall.

3.6.1. SW1 and TW1

In order to evaluate the viability of the floor AR detailing, the strains of the U-shaped reinforcement on the west side of test specimens SW1 and TW1, along with their adjacent reinforcements, were compared, as depicted in Figures 16 and 17. Figure 16e indicates that, for specimen SW1, the strain of U-shaped steel bar SW1-1# and its adjacent floor steel bar(2#, 3#, 4#) increased steadily at the initial loading stage. However, after the load exceeded 80kN, the strain of SW1-1# started to surpass that of SW1-2#, and it reached yield prior to the negative yield load of 111.70kN, without a sudden drop in strain throughout the process. In contrast, Figure 17 reveals that, unlike test specimen SW1, the strain growth of U-shaped steel bars (5#, 8#) almost coincided with adjacent slab steel bars (6#, 9#) during the initial loading phase. However, after the negative load reached 80 kN, the strain growth of U-shaped steel bars started to lag behind adjacent slab steel bars. Although the U-shaped steel bar of test specimen TW1 exhibited strain hysteresis during the loading process, the strain of U-shaped steel bars in the middle and end structural areas was able to withstand a negative yield load of 114.17 kN. The above strain variation patterns demonstrated that U-shaped bars not only have an anchoring and tensile effect similar to that of adjacent slab bars but also function fully in their own right before the specimen yields.

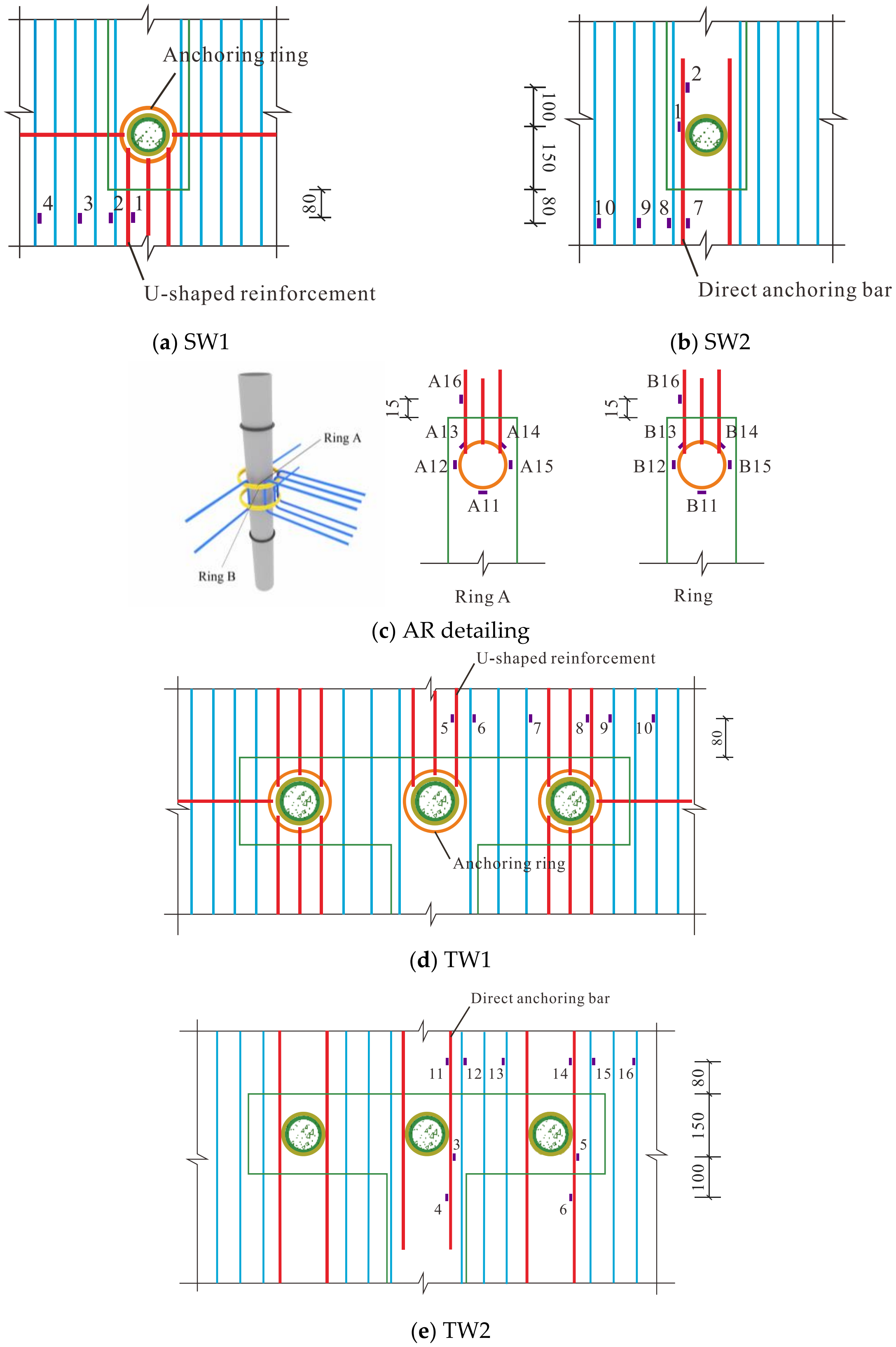

Figure 15. Monitoring point layout of specimens (unit: mm).

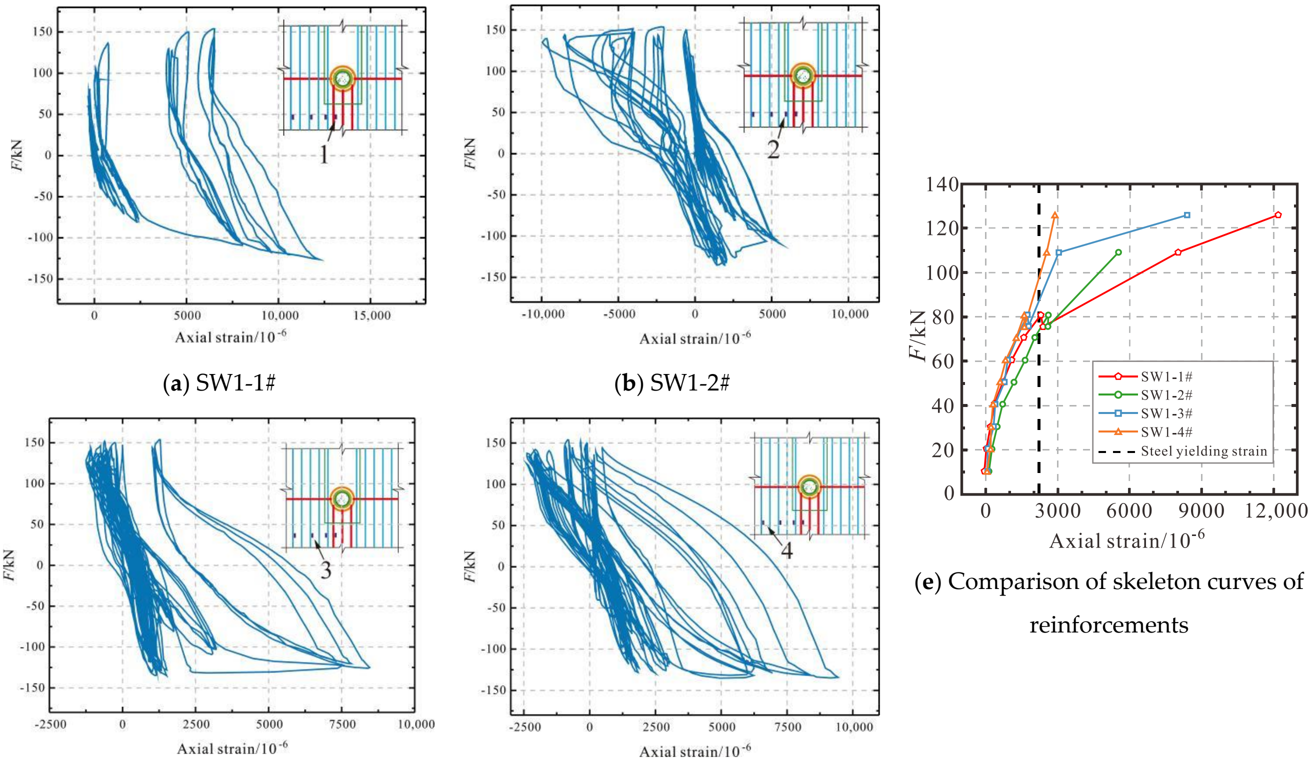

(**a**) SW1-1# (**b**) SW1-2# (**c**) SW1-3# (**d**) SW1-4# (**e**) Comparison of skeleton curves of reinforcements

Figure 16. Hysteretic curves of the lateral load versus reinforcement strain of specimen SW1.

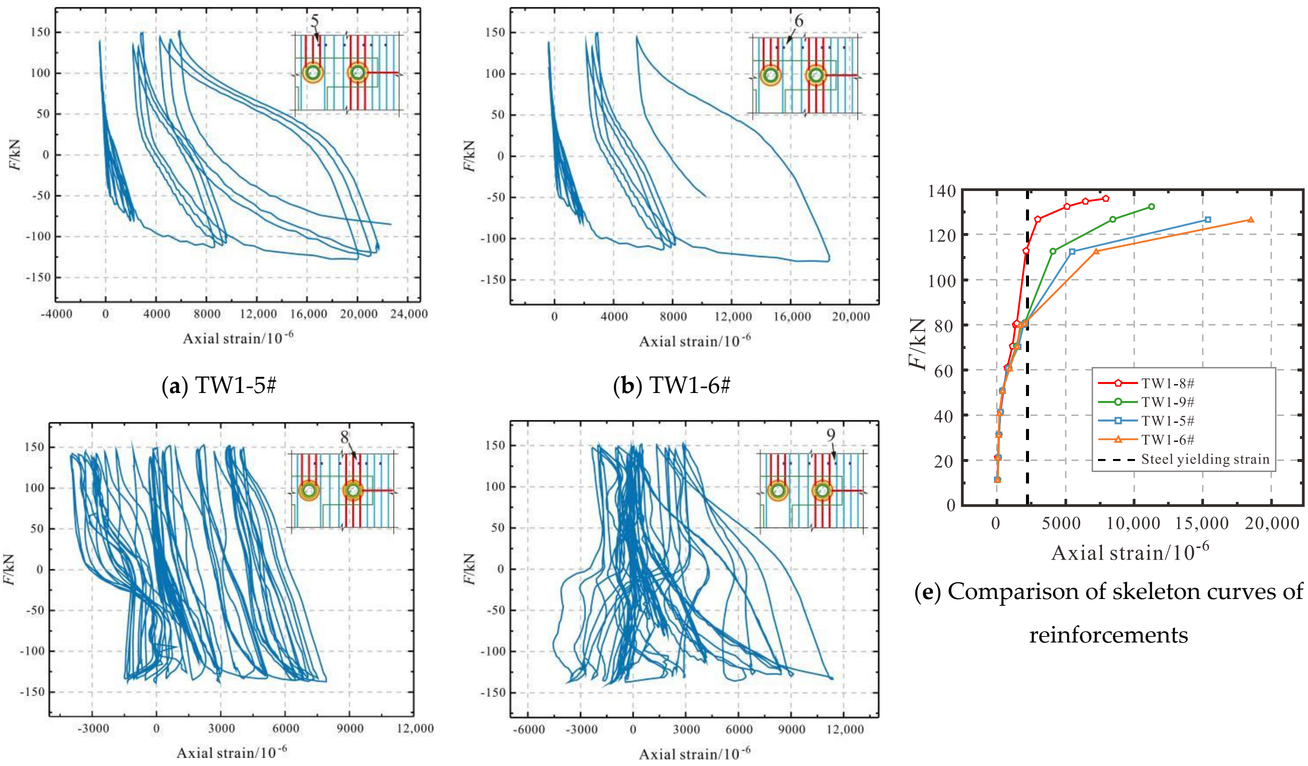

(**a**) TW1-5# (**b**) TW1-6# (**c**) TW1-8# (**d**) TW1-9# (**e**) Comparison of skeleton curves of reinforcements

Figure 17. Hysteretic curves of the lateral load versus reinforcement strain of specimen TW1.

Figure 18 presents the strain analysis of the steel anchor ring of specimen SW1. Due to the similarity of the strain changes between test pieces TW1 and SW1, the latter is used as an example for analysis. As seen in Figure 18f, before loading the forward load of 40kN, the growth of U-shaped steel bar SW1-A16# and of the steel anchor ring (A13#, B13#, A12#, A11#) are almost the same. As the load approaches the normal yield load of 115.01kN, the strain of steel anchor ring bars (A13#, A12#, A11#) decreases successively. This indicates that the closer the location of the U-shaped reinforcement fastening point of the slab, the greater the strain on the AR bars, and vice versa. This proves that the force transmission path of the AR reinforcement is clear and that the U-shaped bars can better transmit the tensile force of the slab steel bar into the interior of the shear wall. Additionally, the strain of AR bar A13# was greater than that of B13#, indicating that the reinforcing steel AR near the floor surface grew faster than the one further away. At the nearly achieved peak load of 153.85 kN, the closest point to the fastening, SW1-A13#, reached yield. These results demonstrate that the AR detailing can transmit force and anchor well during loading, without premature yield and failure.

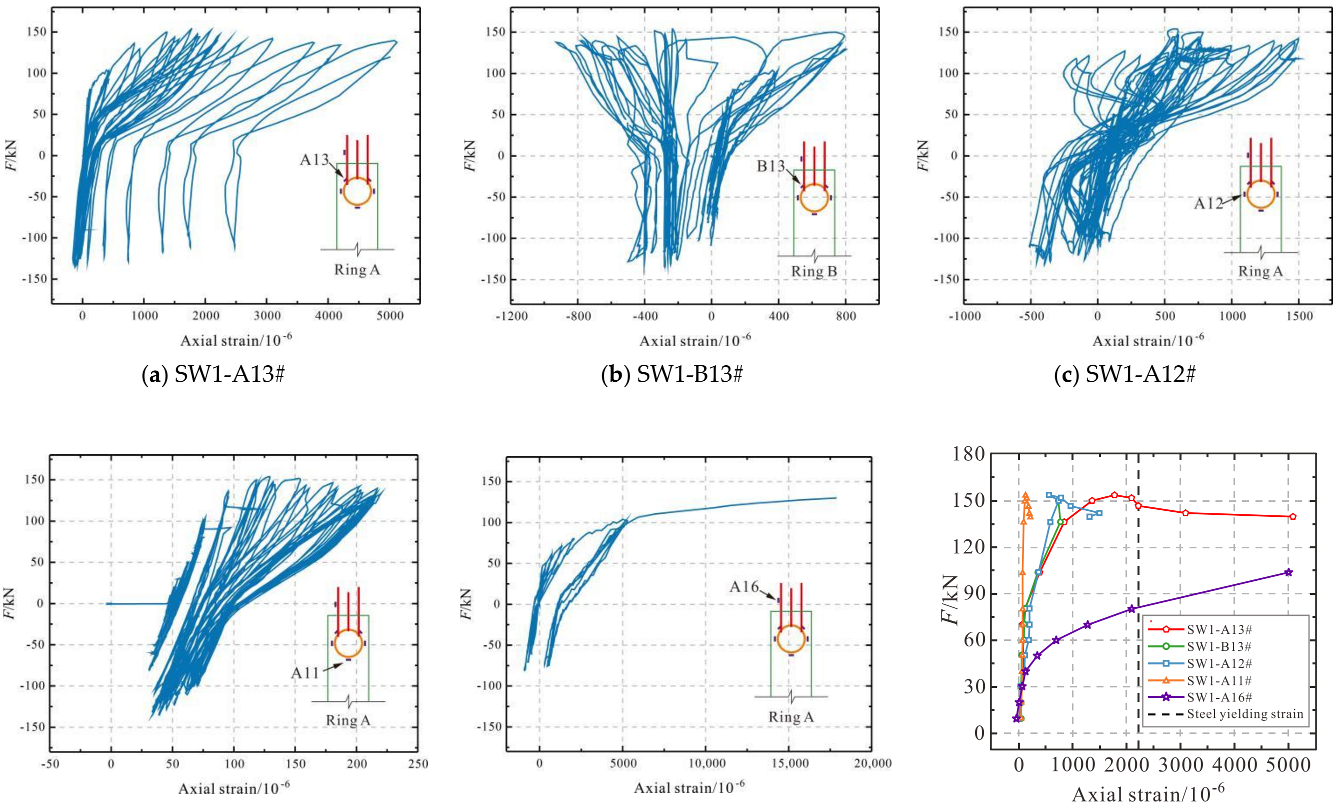

(**a**) SW1-A13# (**b**) SW1-B13# (**c**) SW1-A12#

(**d**) SW1-A11# (**e**) SW1-A16# (**f**) Comparison of skeleton curves of reinforcements

Figure 18. Hysteretic curves of the AR bars of specimen SW1.

3.6.2. SW2 and TW2

In order to analyze the feasibility of the DA detailing, the strains of the direct anchoring steel bar on the west side of the test pieces SW2 and TW2, and its adjacent steel bars of slab, were compared, as depicted in Figures 19 and 20.

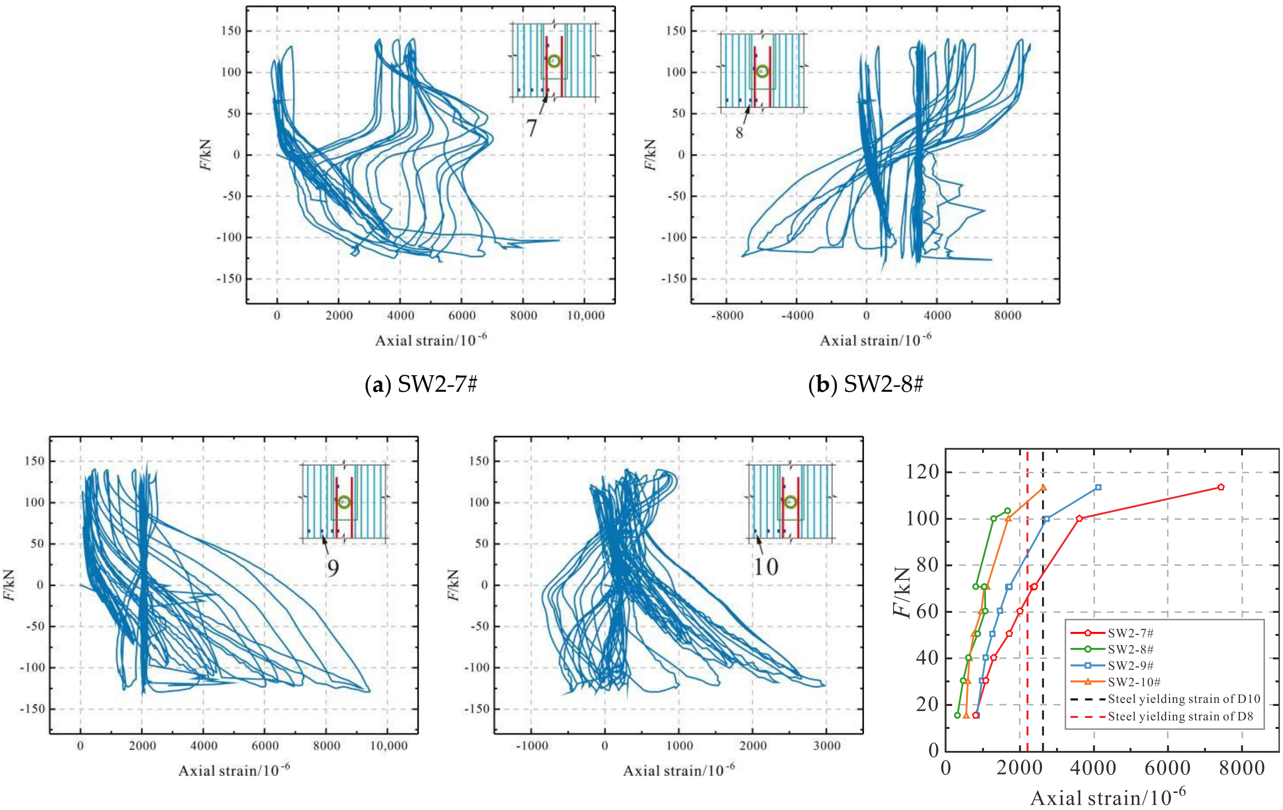

(**a**) SW2-7# (**b**) SW2-8#

(**c**) SW2-9# (**d**) SW2-10# (**e**) Comparison of skeleton curves of reinforcements

Figure 19. Hysteretic curves of the lateral load versus reinforcement strain of specimen SW2.

As shown in Figure 19e, for the specimen SW2, the strain growth of the slab DA steel bar SW2-7# was ahead of the adjacent slab steel bars (8#, 9#, 10#). The DA steel bar reached the negative yield before the load of 104.45kN, explaining that the tensile force of each DA steel bar (D = 10 mm, A = 78.5 mm^2) was greater than 1.5 floor steel bars (D = 8 mm, A = 50.3 mm^2). This shows that the two steel bars of the DA detailing can meet the design intention of bearing capacity of three slab steel bars.

Figure 20 indicates that, in contrast to specimen SW2, the strain of the steel bar in specimen TW2 remained relatively stable during the entire loading process. This is due to the fact that specimen TW2 had a larger support range at the base of the floor, resulting in better support and smoother operation during the loading process. When specimen TW2 reached a positive yield load of 133.18kN, the strain growth of the DA steel bars (11#, 14#) was similar to that of the adjacent floor steel bar (12#, 15#). Based on this observation, we can infer that the tensile force of each DA steel bar was approximately equivalent to that of 1.5 slab steel bars. This finding also supports the design intent of the DA detailing. The above results indicated that the slab DA steel bar can have similar working performance as the adjacent floor steel bar.

Figure 21 presents the strain analysis of the DA steel bar of specimen SW2. Due to the similarity of the strain changes between test pieces TW2 and SW2, the latter is used as an example for analysis.

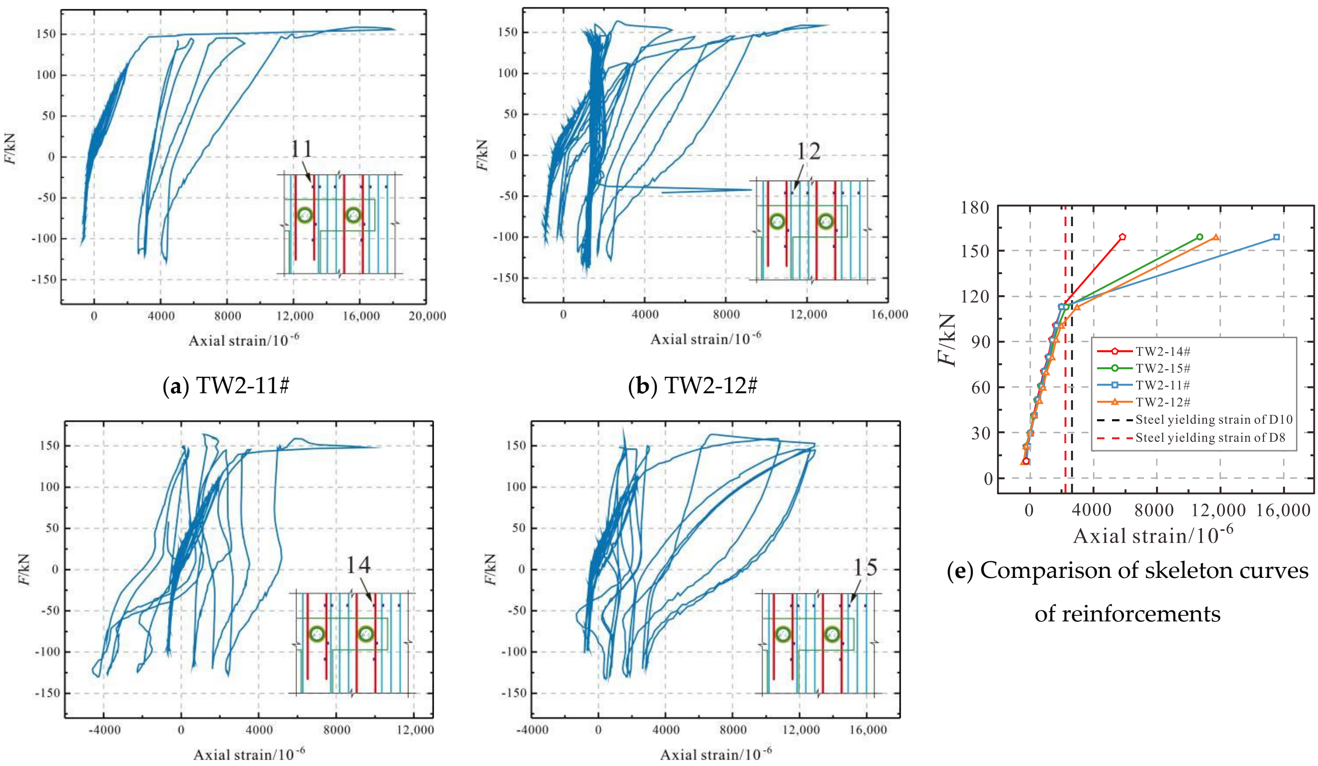

(**a**) TW2-11#

(**b**) TW2-12#

(**c**) TW2-14#

(**d**) TW2-15#

(**e**) Comparison of skeleton curves of reinforcements

Figure 20. Hysteretic curves of the lateral load versus reinforcement strain of specimen TW2.

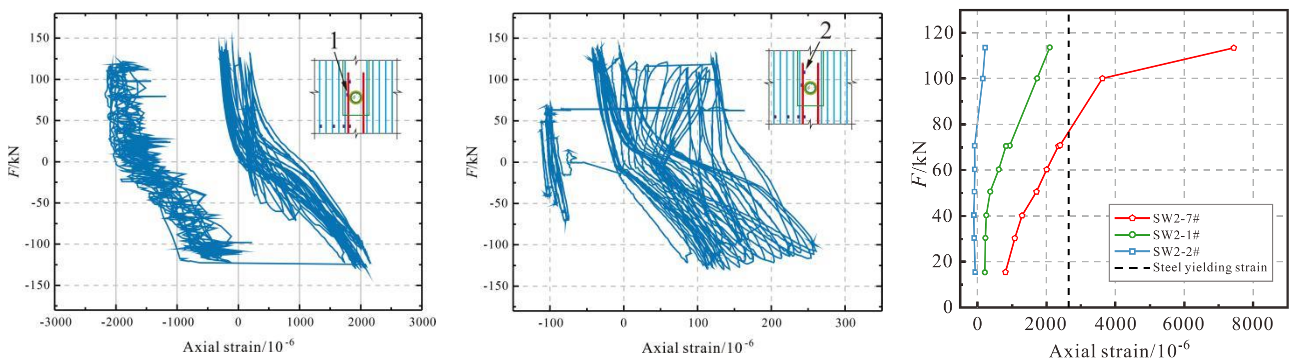

(**a**) SW2-1#

(**b**) SW2-2#

(**c**) Comparison of skeleton curves of reinforcements

Figure 21. Hysteretic curves of the DA bars of specimen SW2.

The strain gauge distribution revealed that SW2-7# was not anchored to the shear wall, and the anchoring length of SW2-1# was 150 mm, whereas that of SW2-2# was 250 mm. Strain analysis of the DA steel bar in Figure 21 demonstrated that the steel bar's strain decreased with the increase in anchoring length. This indicates that the tensile force of the DA reinforcement can be effectively transmitted to the shear wall.

In general, the stress of the reinforcement increased steadily with the strain throughout the loading process, without a sudden drop in strain. The reinforcing steel of each anchorage detailing, AR and DA, near the floor surface grew faster than the one further away. The slab steel bar could reach the yield strength before the failure of the specimen, which provided sufficient lateral stiffness for the specimen.

4. Conclusions

In this paper, two types of no-through-tube anchorage detailing for steel bars in slabs that intersect with CFST-strengthened structural walls are proposed. It also investigates the cyclic behavior of I-shaped and T-shaped CFST-strengthened slab–wall structures with AR and DA detailing. The research involved the establishment and testing of four connection specimens under constant axial load and cyclic reversals. The parameters of resistance such as ductility coefficient, ultimate strength, energy dissipation, and stiffness have been obtained from the test. The following conclusions were drawn from the study:

(1) The specimen, TW1, with T-shaped shear wall and AR detailing has a highest ductility coefficient of 7.87, which demonstrates satisfactory ductility and seismic performance. Other specimens do not yield prematurely during loading, exhibiting reliable anchoring performance.
(2) The stiffness degradation trend is not significantly influenced by the form of the shear wall or the structural configuration of the joint.
(3) When the same detailing was adopted, the seismic performance of the T-shaped shear wall was clearly better than the I-shaped shear wall.
(4) In terms of force transmission and anchorage, the DA detailing was more direct, while the AR detailing was stronger in terms of delaying joint damage and energy consumption. The choice of which to use would depend on the specific requirements of a project.

Author Contributions: Conceptualization, F.W. and X.-D.F.; methodology, K.-M.C., H.-M.Z., X.-S.L. and F.W.; software, K.-M.C., H.-M.Z. and X.-S.L.; validation, K.-M.C., H.-M.Z. and X.-S.L.; formal analysis, K.-M.C., H.-M.Z., X.-S.L. and F.W.; investigation, K.-M.C. and F.W.; resources, F.W.; data curation, F.W. and X.-D.F.; writing—original draft preparation, K.-M.C.; writing—review and editing, F.W.; visualization, K.-M.C. and F.W.; supervision, F.W.; project administration, F.W.; funding acquisition, K.-M.C. and F.W. All authors have read and agreed to the published version of the manuscript.

Funding: This research was funded by State Key Laboratory of Subtropical Building Science, South China University of Technology, grant number 2017KC18.

Data Availability Statement: Data sharing is not applicable to this article.

Acknowledgments: The authors thank Xie-Sheng Li for his assistance in this study during pursuing his master's degree.

Conflicts of Interest: The authors declare no conflict of interest.

References

1. Brunesi, E.; Peloso, S.; Pinho, R.; Nascimbene, R. Cyclic tensile testing of a three-way panel connection for precast wall-slab-wall structures. *Struct. Concr.* **2019**, *20*, 1307–1315. [CrossRef]
2. Brunesi, E.; Peloso, S.; Pinho, R.; Nascimbene, R. Cyclic testing of a full-scale two-storey reinforced precast concrete wall-slab-wall structure. *Bull. Earthq. Eng.* **2018**, *16*, 5309–5339. [CrossRef]
3. Brunesi, E.; Peloso, S.; Pinho, R.; Nascimbene, R. Cyclic testing and analysis of a full-scale cast-in-place reinforced concrete wall-slab-wall structure. *Bull. Earthq. Eng.* **2018**, *16*, 4761–4796. [CrossRef]
4. Qian, J.; Jiang, Z.; Ji, X. Behavior of steel tube-reinforced concrete composite walls subjected to high axial force and cyclic loading. *Eng. Struct.* **2012**, *36*, 173–184. [CrossRef]
5. Fang, X.D.; Jiang, B.; Wei, H.; Zhou, Y.; Jiang, Y.; Lai, H. Axial compressive test and study on steel tube confined high strength concrete shear wall. *J. Build. Struct.* **2013**, *34*, 100–109. (In Chinese)
6. Fang, X.D.; Wei, H.; Li, F.H. Study on axial bearing capacity of shear wall with steel tube confined high-strength concrete. *J. Build. Struct.* **2016**, *37*, 11–22. (In Chinese)
7. Fang, X.D.; Li, Q.; Wei, H.; Zhou, Y.; Jiang, Y.; Lai, H. Experimental study on axial-flexural behavior of shear walls with steel tube-confined high performance concrete. *J. Build. Struct.* **2013**, *34*, 72–81. (In Chinese)
8. Fang, X.D.; Wei, H.; Liu, Q. Experimental study on Seismic behavior of shear walls with steel tube-confined high strength concrete. *J. Build. Struct.* **2015**, *36*, 1–8. (In Chinese)
9. Zhou, J.; Fang, X.; Yao, Z. Mechanical behavior of a steel tube-confined high-strength concrete shear wall under combined tensile and shear loading. *Eng. Struct.* **2018**, *17*, 1673–1685. [CrossRef]

10. Ji, X.; Sun, Y.; Qian, J.; Lu, X. Seismic behavior and modeling of steel reinforced concrete (SRC) walls. *Earthq. Eng. Struct. Dyn.* **2015**, *44*, 955–972. [CrossRef]
11. Wu, L.; Tian, Y.; Su, Y.; Chen, H. Seismic performance of precast composite shear walls reinforced by concrete-filled steel tubes. *Eng. Struct.* **2018**, *16*, 272–283. [CrossRef]
12. Zhou, J.; Li, P.; Guo, N. Seismic performance assessment of a precast concrete-encased CFST composite wall with twin steel tube connections. *Eng. Struct.* **2020**, *207*, 110240. [CrossRef]
13. Zhao, X.Y.; Fang, X.D.; Wang, F.; Zhou, J. Shaking Table Tests of a Novel Flat Slab-Flanged Wall (FSFW) Coupled System with Embedded Concrete-Filled-Steel-Tubes in Wall Piers. *Buildings* **2022**, *12*, 1441. [CrossRef]
14. Wu, Y.F.; Yi, W.J. State-of-the-art on seismic performance of reinforced concrete slab-column structure. *J. Build. Struct.* **2018**, *39*, 45–54. (In Chinese)
15. *GB50010-2010*; Code for Design of Concrete Structures. China Architecture and Building Press: Beijing, China, 2010.
16. *GB/T 228.1-201*; Tensile Tests for Metallic Materials—Part 1: Test Method at Room Temperature. Standards Press of China: Beijing, China, 2010.
17. *JGJ 101-1996*; Code for Seismic Test Methods of Buildings. China Architecture and Building Press: Beijing, China, 1996.
18. Zhang, H.M.; Lv, X.L.; Lu, L.; Cao, H.Q. Influence of boundary element on seismic behavior of reinforced concrete shear walls. *Earthq. Eng. Eng Vib.* **2007**, *27*, 92. (In Chinese)
19. Todut, C.; Dan, D.; Stoian, V. Theoretical and experimental study on precast reinforced concrete wall panels subjected to shear force. *Eng. Struct.* **2014**, *80*, 323–338. [CrossRef]
20. Park, R.; Priestley, M.N.; Gill, W.D. Ductility of square-confined concrete columns. *J. Struct. Div.* **1982**, *108*, 929–950. [CrossRef]
21. Zhou, J.; Zhi, X.; Fan, F.; Jiao, A.; Qian, H. Experimental and numerical investigation on failure behavior of ring joints in precast concrete shear walls. *Adv. Struct. Eng.* **2020**, *23*, 118–131. [CrossRef]
22. Qiao, Q.; Cao, W.; Li, X.; Dong, H.; Zhang, W.; Yin, F. Seismic behavior of shear walls with boundary CFST columns and embedded multiple steel plates: Experimental investigation. *Eng. Struct.* **2018**, *160*, 243–256. [CrossRef]

Disclaimer/Publisher's Note: The statements, opinions and data contained in all publications are solely those of the individual author(s) and contributor(s) and not of MDPI and/or the editor(s). MDPI and/or the editor(s) disclaim responsibility for any injury to people or property resulting from any ideas, methods, instructions or products referred to in the content.